13th International Symposium on Particle Image Velocimetry – ISPIV 2019
Munich, Germany, July 22-24, 2019

Linear Cascade 3D Flow Measurement with Single-camera Light-field PIV

Shengming Xu[1], Di Mei[1], Junfei Ding[1], Shengxian Shi[1*], Hefei Li[2], You Liu[2], Bin Jiang[2]

[1] Shanghai Jiao Tong University, School of Mechanical Engineering, Shanghai, China

[2] Harbin Engineering University, College of Power and Energy Engineering, Harbin, China

[*] kirinshi@sjtu.edu.cn

Abstract

This paper presents an application of light-field PIV (LF-PIV in short) for 3-D resolution of corner separation flow near some linear blade cascade. The experiments were conducted using a subsonic wind tunnel which was running at roughly 70m/s through a blade cascade without a tip clearance. Volumetric laser beams illuminated the seeded tested volume and a LF camera was mounted above the suction surface of the trailing edge for image acquisition. Experiments under different AOAs with different blade heights were performed. The measuring volume for a single case has a size of 39(chordwise)×26(pitchwise)×17(height)mm. More than 200 3-D velocity fields are calculated for a single case and are then averaged for further analysis. The flow structure is assumed to be symmetric about 50% blade height. The authors display in this paper reasonable results at AOA = 10° and blade height from 41% to 98% where the corner separation and end-wall effect is observed. The goal of this study is to extend the usage and investigate the feasibility of 3-D LF-PIV in cascade flow which is a typical space-constrained case and to inquire into the structure of cascade flow.

1 Introduction

The three-dimensional flow characteristics around compressor blade are of great significance in studying the mechanism of compressor stall, surge or instability process. Among them, corner separation is referred to as a typical phenomenon that features the separation and interaction of boundary layers developing on the suction surface and the end-wall. Caused by adverse pressure gradient, it serves a major role in the occurrence of total pressure loss and the consequent stall or even surge. Numerous researches have been conducted upon numerical simulations and 2D PIV experiments of cascade flow. Wernet (2000) concluded requisites for the use of 2D DPIV in turbomachinery. The main methodology includes LDV and PIV. Palafox et al. (2007) applied PIV test in a large-scale turbine blade cascade which is an easier case for optical observation. Corner separation is one of the most important flow structures in compressor blades with intense 3-D complexity. Very few 3-D experimental measurements, however, are conducted due to the difficulty in mounting multiple cameras given limited optical access and test regions. Yu and Liu (2007) employed two cameras for stereo-PIV test in an axial compressor stage while Klinner and Willert (2013) applied four cameras for tomographic PIV in a linear compressor cascade. Both of them suffer from a narrow depth of field and multiple imaging devices. To resolve the volumetric flow field in such a space-constraint case, a monocular LF-PIV system is applied for acquiring 3-D velocity field. LF-PIV has been proved by Fahringer et al. (2015) and Shi et al. (2018)Shi et al. (2016) to be capable of resolving 3-D velocity field. And it has been successfully applied in many practical experiments such as a supersonic jet by Ding et al. (2018) and a leading-edge vortex by Wabick et al. (2018).

This paper will give an introduction to the principle of LF-PIV in Section 2 and detail the experiments and data analysis on a linear cascade in Section 3, followed by a conclusion in Section 4.

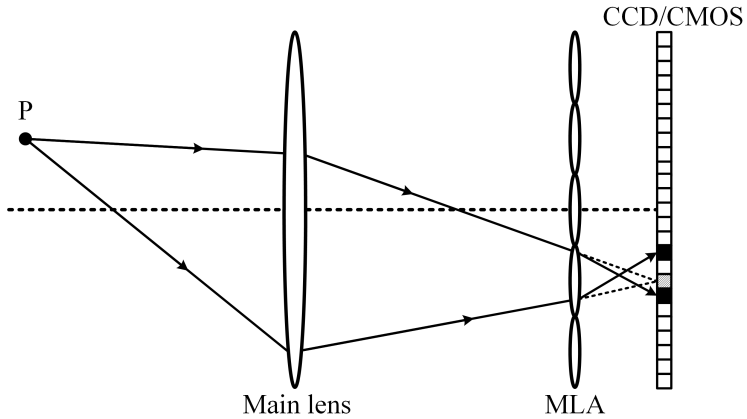

Figure 1: Schematics of a ligh-field camera

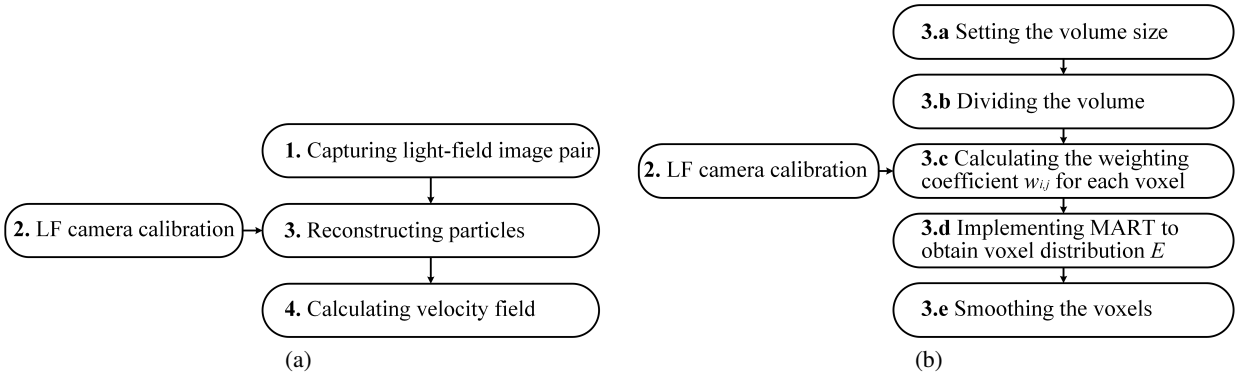

Figure 2: Flow chart of (a) Light-field PIV and (b) particle reconstruction

2 Principles of Light-field PIV

The term 'light-field' refers to a concept to represent the complete information of rays. In the field of computational photography, light-field imaging is gaining ever-increasing attention with the updating and elevation of computing power as a monocular system for 3-D information resolving. A light-field camera exploits a micro-lens array (MLA) installed parallel and in front of the sensor plane for gaining angular information of light which is lost due to defocusing patterns in a conventional camera. This effect is demonstrated in Figure 1 where the light paths of two example rays from a point source P are described as solid lines through a simplified architecture of the light-field camera. The dashed lines converging at a single pixel are original directions of rays at the absence of the MLA while the two rays reach two different pixels in this specially designed device architecture. The separation of rays from distinct directions enable the reconstruction of 3-D voxel fields which is the key step in LF-PIV.

A general flow chart for the framework of LF-PIV is exhibited in Figure 2(a). The detailed steps in reconstructing voxel fields are shown in Figure 2(b). The overall graphical interpretation is displayed as Figure 3. Same as Tomo-PIV in resolving 3-D velocity field, for LF-PIV, the measuring region seeded with tracer particles is illuminated with a volumetric laser beam. A light-field camera is applied to the acquisition of particle image pairs for the volume of interest. For each particle image, 3-D distribution of voxel intensity in a certain volume is calculated. In recent years, various approaches to the reconstruction of particles have been studied. Among them, the multiplicative algebraic reconstruction is verified as feasible by previous studies (Fahringer et al. (2015); Shi et al. (2017, 2016)). A calibration process for LF-PIV is conducted following the work by Shi et al. (2019), which corrects errors in camera intrinsic parameters and distortion induced by the imperfect optical elements as well as their installation. Then, an FFT-based normalized cross-correlation will be implemented on the two consecutive frames of voxels for calculating

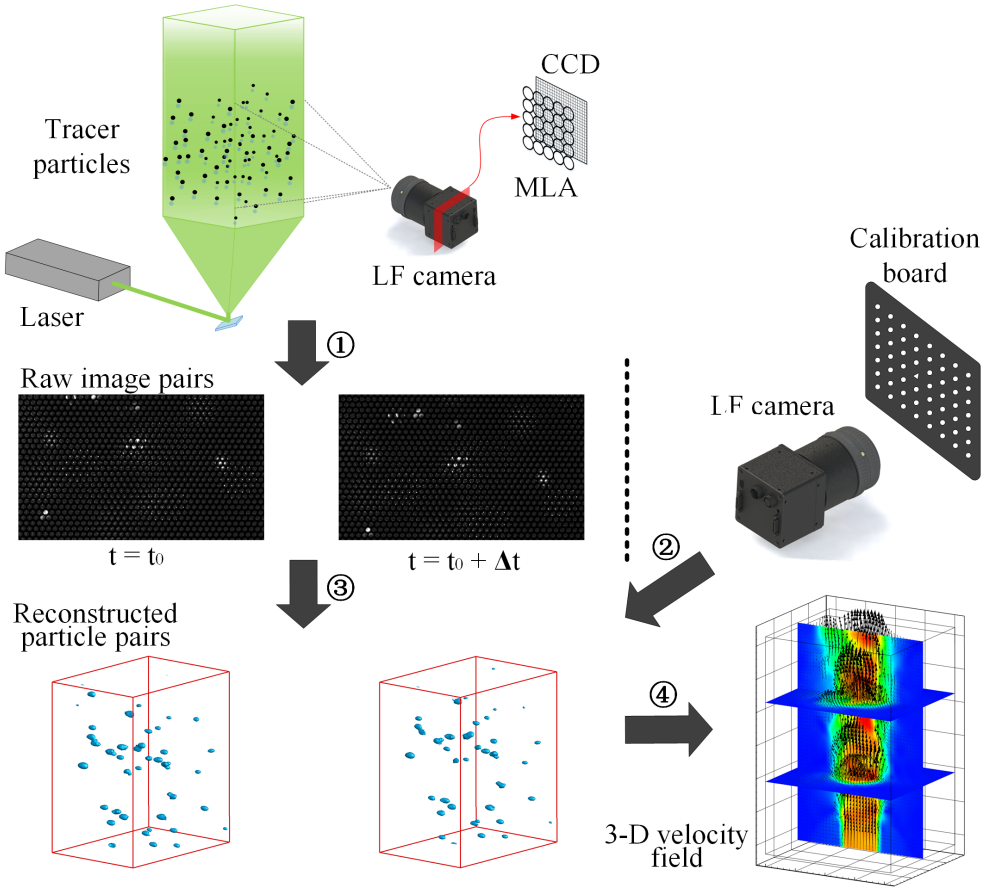

Figure 3: Graphical flow chart

the 3-D velocity distribution under a known time interval. The detailed steps in reconstructing particle location will be explained in the rest of this section.

Assume the object space coordinate system to be $X-Y-Z$, and the image coordinate system to be $U-V$. In the first place, the volume of interest is selected as a cuboid with a known size (step 3.a in Figure 2(b)). The cuboid is usually centered at the origin of the object space where plane $z=0$ denotes the plane of focus (POF). Then, the volume is uniformly divided into voxels (step 3.b) upon which the voxel intensity will be reconstructed. The weighting coefficient for a voxel is written as:

$$w_{i,j} = w\left(x_i, y_i, z_i, u_j, v_j\right) \tag{1}$$

which is calculated for each voxel (step 3.c) by means of a ray tracing method (Shi et al. (2016)). The propagation of light can be simulated as a series of propagation matrix under a non-wave-optics condition. An example of the weighting coefficient for a specific voxel is shown in Figure 4. The red dashed circles are the rims of the involved micro-lenses and the grey pixels are the representation of relative pixel intensity. The magnitude of pixel intensity is equivalent to the relative amount of light a pixel has received. Denote the pixel intensity at (u,v) as $I_{coef}(u,v)$, and the voxel coordinates as (x_i, y_j, z_k), then the normalized weighting coefficient can be expressed as:

$$w\left(x_i, y_i, z_i, u_j, v_j\right) = \frac{I_{coef}\left(u_j, v_j\right)}{\sum_j I_{coef}\left(u_j, v_j\right)} \tag{2}$$

Further, denote the voxel intensity after the kth iteration as $E(x,y,z)^k$, the MART process (Atkinson and Soria (2009); Worth and Nickels (2008)) can be expressed as:

$$E\left(x_i, y_i, z_i\right)^{k+1} = E\left(x_i, y_i, z_i\right)^k \left(\frac{I_{img}\left(u_j, v_j\right)}{\sum_i w_{i,j} E\left(x_i, y_i, z_i\right)}\right)^{\mu w_{i,j}} \tag{3}$$

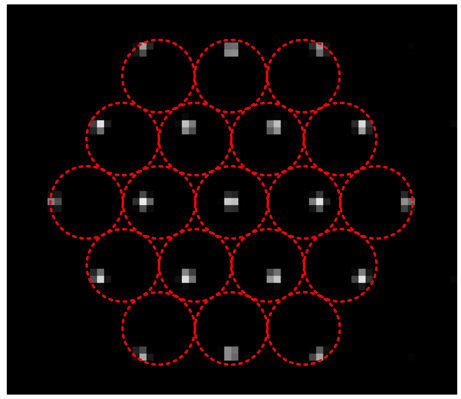

Figure 4: Simulated image of a voxel

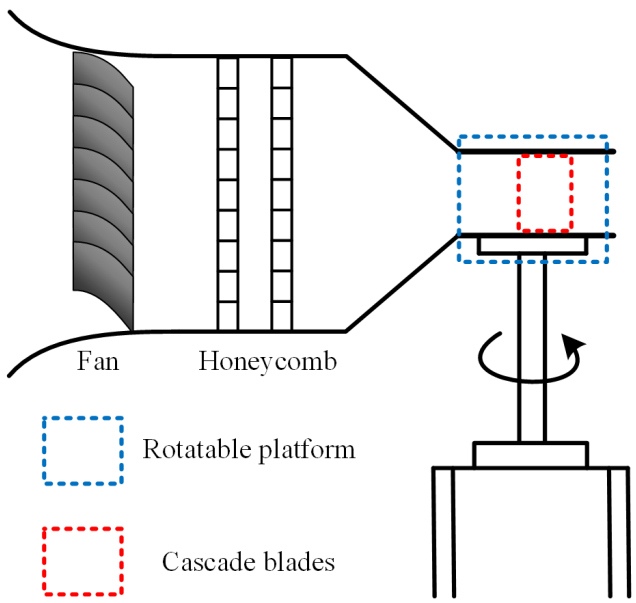

Figure 5: Schematics of the wind tunnel

After the iteration process of MART, the voxel intensity will be smoothed using a 3-D Gaussian filter for noise removal. And the smoothed pairs of voxel fields can be direct inputs of the 3-D cross-correlation in calculating velocity fields.

3 Experiments on a Linear Cascade

The experiment was conducted upon some linear cascade blades at the outlet of a wind tunnel. Schematics of the tested linear cascade and test configurations are presented in Figure 5 and 6. Table 1 explains some of the blade parameters. The wind tunnel can run at a maximum power of 30kW, corresponding to wind velocity before the leading edge of around 70m/s. The Reynolds number is around 3.6×10^5 based on the entrance velocity and the blade chordlength. The blade cascade consists of 11 identical parallel blades aligning in a rotatable platform at the outlet of the wind tunnel. The AOA can be adjusted through the platform. There is acrylic end-wall both at $z/h = 1$ and $z/h = 0$. The volume shown as red wireframes in Figure 6(a) and 6(b) is the region on which light-field images were taken and LF-PIV was performed.

An in-house plenoptic PIV camera (6600 × 4400 pixels, Shi et al. (2016)) was used to capture the image of the volume illuminated with a dual-head 500 mJ/pulse Nd:YAG laser (Beamtech. Vlite-500). The laser beam was adjusted in terms of its cross-section using two cylindrical convex lenses and two cylindrical

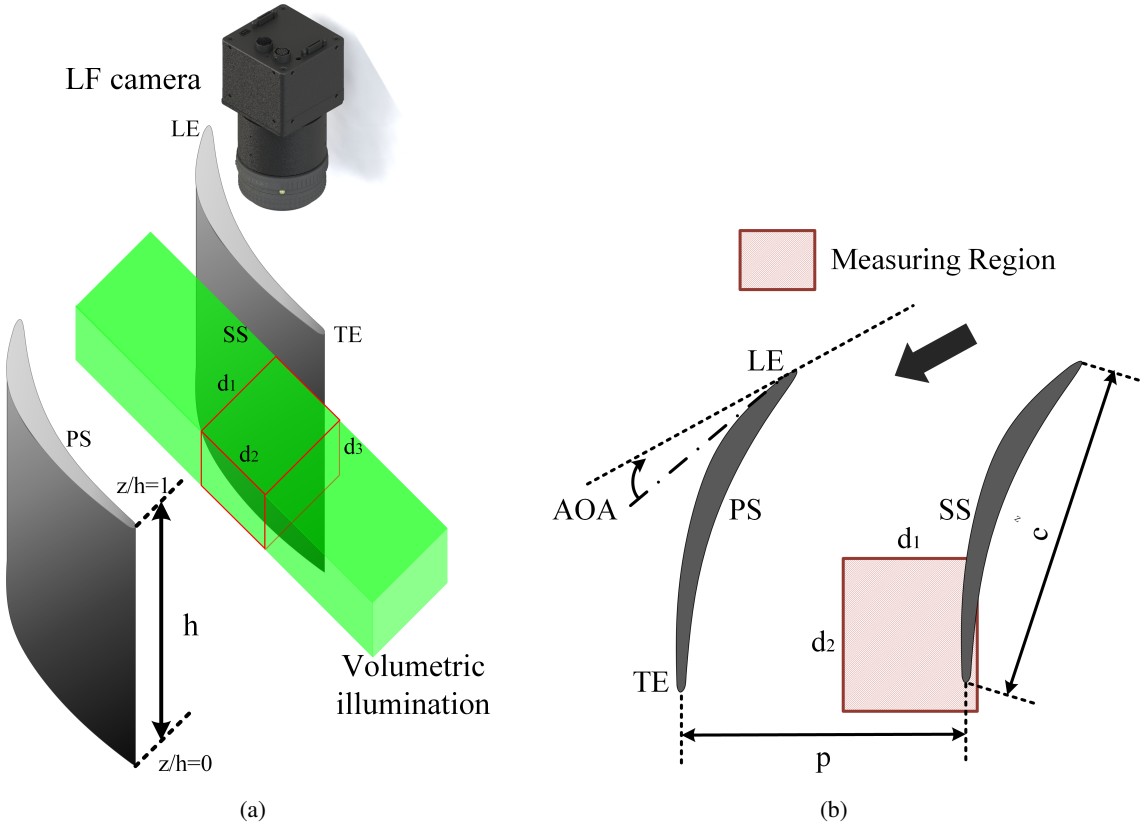

Figure 6: Schematics of the test rigs from its (a) isometric view and (b) top view

Table 1: Explanation of notations

Notation	Name	Value(mm)
h	Blade height	100
p	Blade pitch	52.2
c	Chord length	69.6
$d_1 \times d_2 \times d_3$	Measuring region	$\approx 39 \times 26 \times 17$

concave lenses so that the volume of interest is fully covered. Bis(2-ethylhexyl) sebacate is atomized by high-pressure air to form the seeding particles with a diameter of approximately $1\mu m$. The experiments were conducted under multiple values of AOA at 0°, 2°, 4°, 8°, and 10°, while in this paper, results of the 10° case will be displayed with a further discussion. 500 image pairs were taken out of which more than 200 image pairs were selected for the eventual calculation of velocity field. The selection is based on a particle density threshold because the density was fluctuating during the running of the wind tunnel. A volume with a size of $39 \times 26 \times 17cm^3$ is partitioned into $2200 \times 1466 \times 320$ voxels. The interrogation window was finally $64 \times 64 \times 32$ voxels, corresponding to a vector resolution of $1.16 \times 1.16 \times 1.93mm^3/vector$. The instantaneous velocity fields were then averaged for further analysis and will be discussed in the following.

Figure 7 shows the averaged velocity field at AOA = 10°. The result is obtained by joining three experimental cases which are centered at $z/h = 50\%$ $z/h = 70\%$ $z/h = 90\%$ respectively. The height range is from 41% to 98%. The magnitude of velocity is depicted in a color map. 4 slices of $X-Y$ plane and 1 slice of $Y-Z$ plane are plotted in Figure 7(a). The velocity contour is plotted on the $Y-Z$ slice the 4 $X-Y$ slices are displayed in Figure 7(b) with vectors added.

The four sub-figures exhibit velocity distribution at four different z planes. With the increase in blade height, namely, when further approaching the endwall, the overall magnitude of velocity experiences a gradual rise then a sudden drop over $z/h = 90\%$. This is the joint effect of vortices developing along the suction surface and end-wall surface. Theoretical models proposed by Langston (1980) and Sharma and Butler (1987) suggest that end-wall effect will complicate corner separation and intensify breakdown of separation vortex which is the culprit of compressor stall or surge. When being close enough to the end-wall, the flow is mainly dominated by the end-wall boundary layer and appears to be small in its magnitude and vorticity. This can be observed in the plane at $z/h = 95\%$ and the contour lines at the top of the $Y-Z$ slice.

4 Conclusion

This paper has introduced a practical application of LF-PIV in measuring 3-D flow structure in a blade cascade. Averaged results are displayed for AOA = 10° and blade height from 41% to 98%. The consistency between the experiment and the supporting theories have demonstrated the capability of LF-PIV in resolving 3D complex velocity field. The compact and concise monocular system setup makes it especially suitable for space-constraint cases. The future work should be primarily focused on the improvement of measuring accuracy in the depth direction and, if possible, the further application in a real axial compressor.

Acknowledgements

The authors are grateful to Harbin Engineering University for facilitating the experiments. They also appreciate Zhenyi Chen for his tremendous help in accommodating relevant students, setting up apparatus and timely discussion over the research issues.

References

Atkinson C and Soria J (2009) An efficient simultaneous reconstruction technique for tomographic particle image velocimetry. *Experiments in Fluids* 47:553

Ding J, Lim H, Sheikh S, Xu S, Shi S, and New T (2018) Volumetric measurement of a supersonic jet with single-camera. in *19th International Symposium on the Application of Laser and Imaging Techniques to Fluid Mechanics, Lisbon, Portugal*

Fahringer TW, Lynch KP, and Thurow BS (2015) Volumetric particle image velocimetry with a single plenoptic camera. *Measurement Science and Technology* 26:115201

Klinner J and Willert C (2013) Application of tomographic piv in a transonic cascade. in *10th International Symposium on Particle Image Velocimetry, PIV13, Delft, The Netherlands*

Langston LS (1980) Crossflows in a turbine cascade passage. *Journal of Engineering for Power* 102:866–874

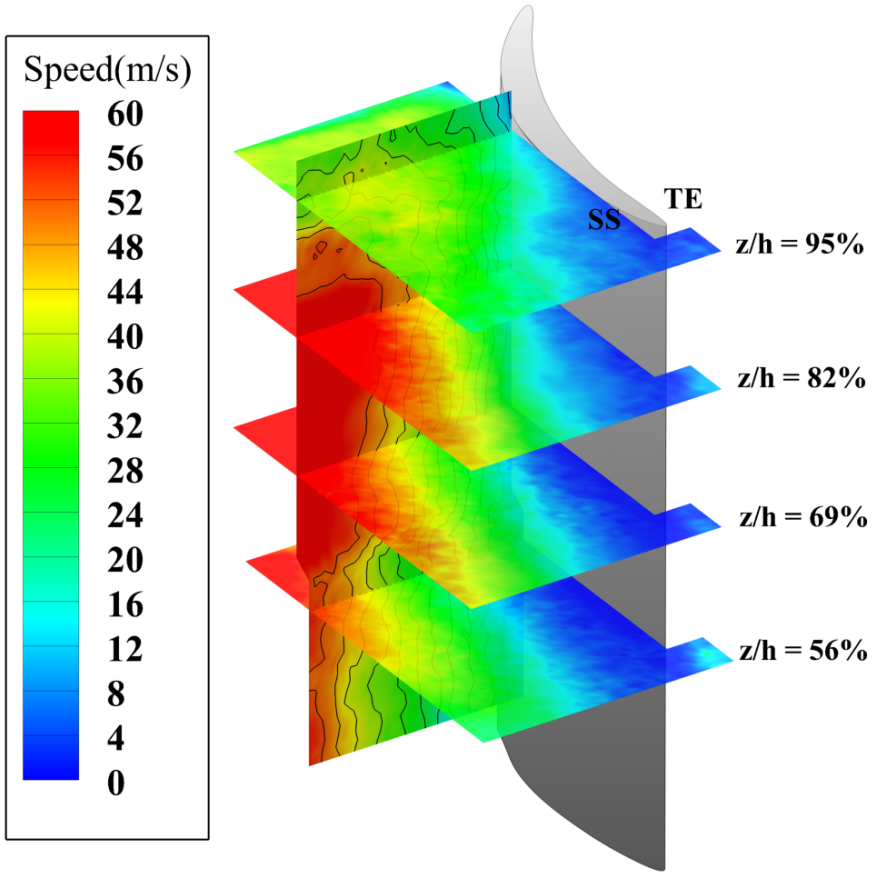

(a)

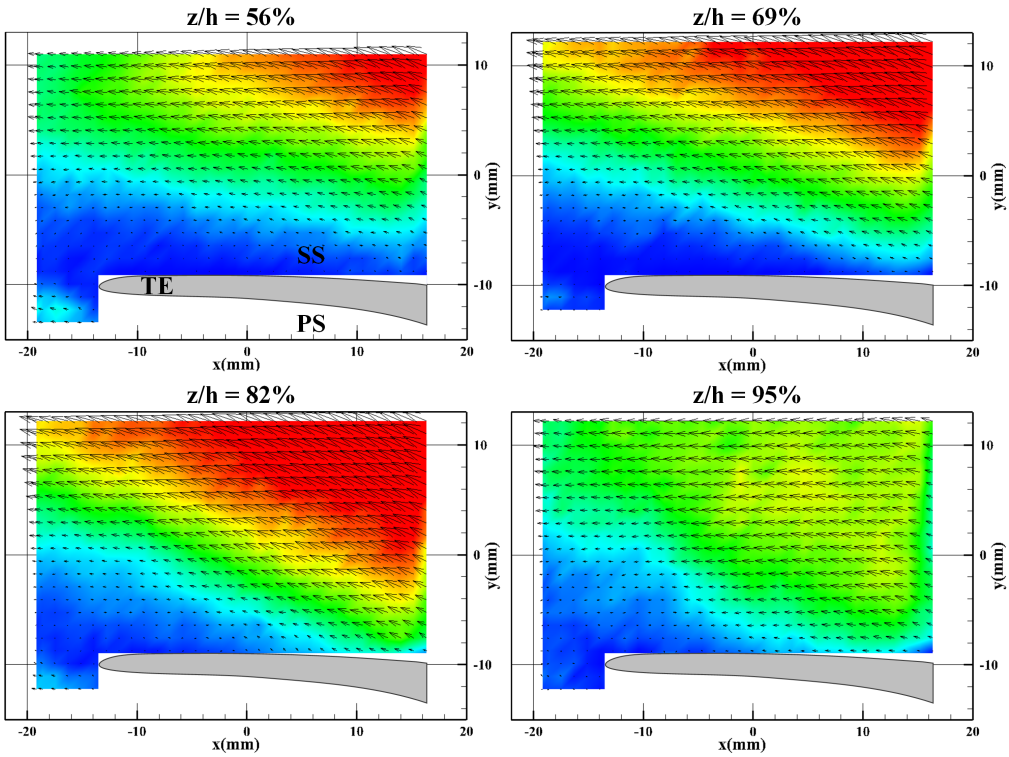

(b)

Figure 7: Averaged velocity field near the suction surface of the trailing edge (AOA = 10°): (a) isometric view, (b) slices at z/h = 56%, 69%, 82% and 95%

Palafox P, Oldfield MLG, LaGraff JE, and Jones TV (2007) Piv maps of tip leakage and secondary flow fields on a low-speed turbine blade cascade with moving end wall. *Journal of Turbomachinery* 130:011001–011001–9

Sharma OP and Butler TL (1987) Predictions of endwall losses and secondary flows in axial flow turbine cascades. *Journal of Turbomachinery* 109:229–236

Shi S, Ding J, Atkinson C, Soria J, and New TH (2018) A detailed comparison of single-camera light-field piv and tomographic piv. *Experiments in Fluids* 59:46

Shi S, Ding J, New TH, Liu Y, and Zhang H (2019) Volumetric calibration enhancements for single-camera light-field piv. *Experiments in Fluids* 60:21

Shi S, Ding J, New TH, and Soria J (2017) Light-field camera-based 3d volumetric particle image velocimetry with dense ray tracing reconstruction technique. *Experiments in Fluids* 58:78

Shi S, Wang J, Ding J, Zhao Z, and New TH (2016) Parametric study on light field volumetric particle image velocimetry. *Flow Measurement and Instrumentation* 49:70–88

Wabick KJ, Buchholz J, Johnson K, and Thurow BS (2018) Characterization of vorticity transport in the leading-edge vortex of a rolling wing using plenoptic piv. in *2018 AIAA Aerospace Sciences Meeting*. page 1292

Wernet MP (2000) Development of digital particle imaging velocimetry for use in turbomachinery. *Experiments in Fluids* 28:97–115

Worth NA and Nickels TB (2008) Acceleration of tomo-piv by estimating the initial volume intensity distribution. *Experiments in Fluids* 45:847

Yu XJ and Liu BJ (2007) Stereoscopic piv measurement of unsteady flows in an axial compressor stage. *Experimental Thermal and Fluid Science* 31:1049–1060